Proc. Arthropod. Embryol. Soc. Jpn. 38, 1–8 (2003)

ISSN 1341–1527

[REVIEW]

Application of the Projection X-ray Microscopy to Biological Specimens

Hideyuki YOSHIMURA

Department of Physics, School of Science and Technology, Meiji University, Higashimita 1–1–1, Tama-ku, Kawasaki, Kanagawa 214–8571, Japan
E-mail: hyoshi@isc.meiji.ac.jp

Abstract

The projection X-ray microscope was constructed by modifying a commercial scanning electron microscope. The resolution of this microscope was about 0.1 μm, little higher than that of an optical microscope. Because the focal depth of this microscope is long, the whole area of a thick sample (about 3 mm) can be focused. Micrographs of various biological samples are presented, which demonstrate that our X-ray microscope is a very useful tool for the nondestructive studies of internal structures of small insects and histological studies of thick preparations.

Introduction

The projection X-ray microscope makes use of a very small X-ray source from a thin (0.1–3 μm) target metal film that is excited by a focused electron beam. If an object is placed just below the target metal film, the diverging X-rays enlarge the shadow of the object. Because of this principle, focal depth can be infinite. The long focal depth is advantageous for the analysis of bulky samples (thicker than 3 mm). This type of X-ray microscope was developed as a shadow projection X-ray microscope in the 1950s (Cosslett and Nixon, 1951; Nixon, 1955; Newberry and Summers, 1956) and was further advanced by Newberry (1988) and Yada and Takahashi (1988). Yada and Takahashi (1988) utilized electron beam of a scanning electron microscope (SEM) for exiting a metal target, and it improved focusing process of electron beam to get a fine X-ray source. Nevertheless, this device has not developed into a popular X-ray microscope because of its limited resolution and relatively low intensity of the X-ray source. However, recent advances in electronic technology have overcome these problems. Stability and current density of the electron beam in SEM have improved appreciably, contributing to the production of a strong and stable X-ray source. Also sensitivity of the X-ray CCD camera increased, allowing time-lapsed X-ray imaging even with a weak X-ray intensity (Yoshimura *et al.*, 1997). Therefore, the projection X-ray microscope should be re-considered as an analytical tool at the laboratory level.

Basic structure of projection X-ray microscope

We constructed an X-ray microscope by modifying a HITACHI model S-2500CX SEM, using a transmitting target metal film for the X-ray source (Fig. 1). An LaB_6 cathode was adopted to get a compact electron beam with high electron-current density. Thin target metal film (about 3×3 mm^2, thickness 0.1–3 μm) was fixed so as to cover the 250 μm diameter hole of the bulkhead which separates the vacuum area of SEM optics from the atmospheric sample chamber (Fig. 1b). It was also used as the metal target of the X-ray source. The X-ray from the metal target is composed of continuous and characteristic X-rays. The spectrum depends on the acceleration voltage and the metal target material.

A sample was kept on an XYZ-stage (Fig. 1c) fixed just below the metal target. A silicon nitrite membrane (0.2 μm in thickness, Silson Ltd.) or a thin adhesive tape (0.45 μm in thickness) was used to support the sample on the XYZ-stage. Since the image of the sample is enlarged by the divergence of X-rays, the magnification M is given by

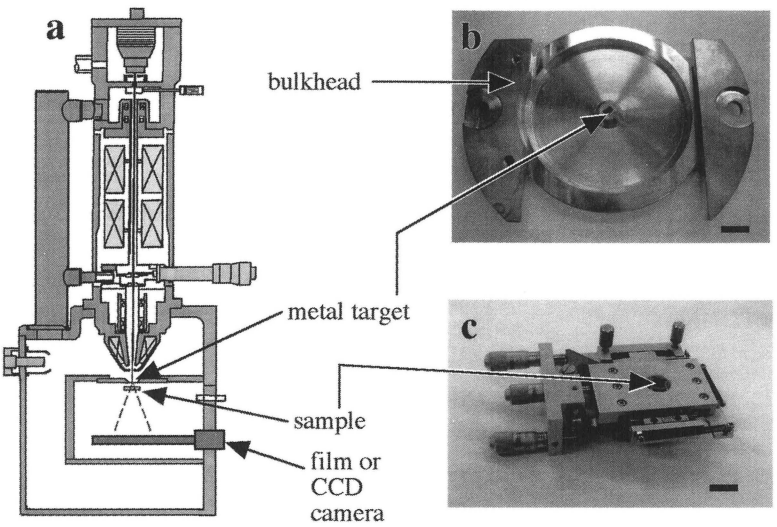

Fig. 1 Basic structure of the projection X-ray microscope. a. Schematic drawing of the microscope. b. The bulkhead which separates the vacuum area of SEM optics from the atmospheric sample chamber. c. An XYZ-stage to support the sample. Scales = 1 cm.

the ratio between the metal target/imaging-device distance D_t, and the metal target/sample distance D_s, thus $M=D_t/D_s$. For low magnification measurements less than $M=20$, the sample was fixed by adhesive tape and D_s was adjusted by a silicon rubber spacer (5–10 mm in thickness).

The sample chamber is sealed so as to allow for exchanging gas in it (Fig. 2). A Polaroid cassette for Type 52 film or home-designed cassette for negative film (4489 electron microscope film, Kodak) can be inserted at the side of the sample chamber (Fig. 2). An X-ray cooled-CCD camera (C4880, Hamamatsu) was also used to record images. Typical exposure times were 10–60 sec for the Polaroid film, and 5–15 min for electron microscope film. Polaroid film was used for testing exposure. Exposure time for the CCD camera was 1–60 sec and sometimes individual images were

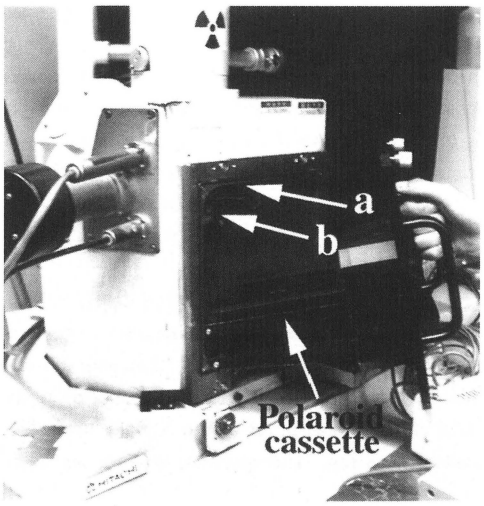

Fig. 2 Sample chamber of the microscope. Polaroid film cassette or cassette for negative film can be inserted at the side of the sealed sample chamber. The bulkhead with metal target and the XYZ-stage are shown by allows a and b, respectively.

integrated to get a better S/N ratio.

The primary factor to determine the resolution of this microscope is the size of the X-ray source. The size of the electron beam can be focused as small as 10 nm in diameter. However, electrons which have penetrated into the metal target are scattered and as a result X-rays are emitted from a wider diffused area. The resolution of this microscope was about 0.1 μm, determined by the X-ray micrograph of the gold grid.

Spectra of the X-rays

The spectrum of the X-rays emitted from the metal target depended on the acceleration voltage of the electron beam and the metal of the target. The spectrum was also influenced by the thickness of the metal target and gas in the sample chamber, because of the absorption effect along the optical path.

Figure 3a, b shows the spectra of X-rays emitted from the gold target with a thickness of 0.3 μm excited by electron beams of 8, 10, 15 and 20 keV acceleration voltages. An Si-PIN photodiode detector (XR-100T, AMPTEK Inc.) placed 100 mm from the X-ray source measured the X-ray spectrum with a multi-channel analyzer (Series 5000, Aptec Eng. Ltd.). The spectra consist of the characteristic X-rays of gold L_α (9.71 keV, 0.128 nm), L_β (11.5 keV, 0.108 nm) and M_α (2.15 keV, 0.584 nm). The peak at 8.1 keV (0.15 nm) is probably the characteristic X-ray of the copper K_α that was used in the bulkhead to fix the gold target film. The characteristic X-ray of M_α (0.584 nm) was seen clearly when the chamber was filled with helium (Fig. 3b), while it was not detected in air (Fig. 3a), because the line absorption coefficient of air at this wavelength is about 0.52 cm^{-1}, which is about 270 times larger than that of helium gas (Lonsdale, 1968). However, the characteristic X-rays of L_α (0.128 nm) and L_β (0.108 nm) were detected in air, because the line absorption coefficient in this wavelength range is sufficiently small (about 7×10^{-3} cm^{-1} at wavelength 0.13 nm) to allow X-rays to penetrate the 100 mm optical path. In Figure 3c, the spectra of X-rays emitted from an aluminum target with thickness of 3 μm excited by electron beams of 8, 10, 15 and 20 keV acceleration voltages are shown. The peak of the characteristic X-ray of aluminum K_α at 1.5 keV (0.834 nm) was dominant, when the chamber was filled with helium gas. Longer wave-length X-ray components have the advantage of contrasting thin biological samples which mainly consist of light elements such as carbon. We usually use gold or platinum targets for thick samples and use aluminum targets for thin samples.

Sample preparation

Living samples can be inspected using this microscope, however detailed structures in the body was not clear, because the contrast between water (body fluid) and organisms is small. To reveal fine structures, samples were dried by the critical-point drying technique (Anderson, 1951). An ant (not identified) and a water flea (*Moina macrocopa*) were fixed with 2.5% glutalaldehyde in 50 mM sodium phosphate buffer (pH 7.2) solution. Water in the solution was exchanged with ethanol by gradually increasing ethanol concentration. Finally ethanol (100%) was replaced with 3-

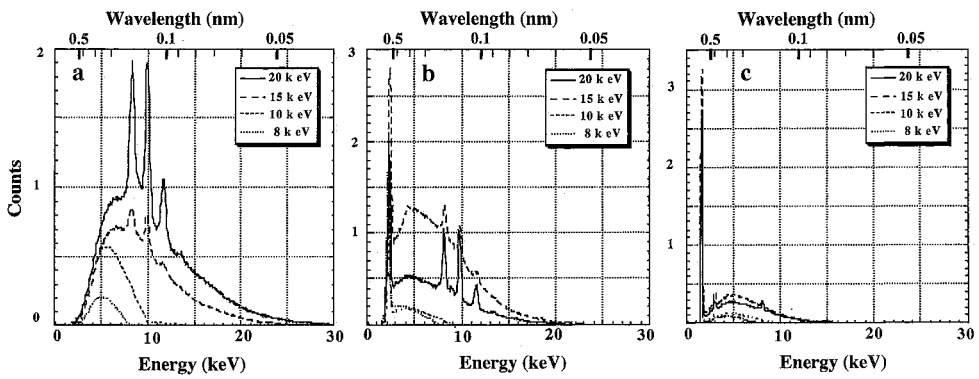

Fig. 3 Spectra of the X-rays. The spectrum was measured using an Si-PIN photodiode detector placed 100 mm from the metal target. The sample chamber was filled with air (a) or helium gas (b, c). The 0.3 μm thick gold target (a, b) or 3 μm thick aluminum target (c) were irradiated with electron beams of 8, 10, 15 and 20 keV acceleration voltages.

methylbutyl acetate and the samples were subjected to critical-point drying. A Golgi-stained section of rat cerebral cortex, a gift from Dr. K. Hama (Hama *et al.*, 1989) was also examined. Here, to obtain more contrast, nerve cells were stained by silver (Golgi-staining).

Contrast

Images obtained by the projection X-ray microscope exhibited enhanced object edges, similar to images produced by an electron microscope in an under-focused state. This phenomenon is explained by the Fresnel edge diffraction, whereupon its amplitude depends on the size of the light source d_x and the distance between the light source and the specimen D_s (Wilkins *et al.*, 1996). The degree of coherence γ, which determines the contrast due to the interference, is close to unity when $d_x/D_s\lambda$ is small (λ, wavelength of the X-ray) (Yoshimura *et al.*, 2000). Therefore the contrast is better, when $D_s\lambda$ is larger. On the other hand, the slope of the edge increases with $\sqrt{D_s\lambda}$ (Nixon, 1955), thus there is an optimum length of D_s to obtain a good contrast with high resolution. For this microscope, experimentally obtained optimum D_s was around 0.5 mm to 2 mm, when the image was recorded in the air atmosphere.

The contribution of longer wavelength X-ray components in recording images became dominant, when the sample chamber was filled with helium gas, since these components were adsorbed in the air (Fig. 3). In a helium gas atmosphere, because $D_s\lambda$ was larger than in the air atmosphere, the edge enhancement effect was significant. Figure 4 shows X-ray micrographs of the thin hairs around an ant leg joint in helium gas and in air. It can be clearly seen from these images that the Fresnel fringes are stronger in helium gas than in air.

Living sample

Because the sample chamber can be filled with an air atmosphere, we can record X-ray micrographs using living samples. Figure 5 shows the metamorphosis of *Drosophila melanogaster* in the same individual during the pupa stage. It is known that there is an intermediate stage where a large part of the body of a larva is fused in a pupa during the metamorphosis of insects. Figure 5a, b shows this process for *Drosophila melanogaster*. Figure 5c shows an X-ray image of an imago fly treated by critical-point drying. The well-developed muscle system needed to drive the alae can be seen.

Figure 6 shows an X-ray image of a grasshopper, *Atractomorpha lata*, in a carbon dioxide atmosphere. The insect can be anesthetized in that atmosphere. Because the focal depth of this microscope is long, the whole area of such a thick sample (about 3 mm) can be focused.

High magnification imaging

As optimum D_s was about 0.5 mm in an air atmosphere, magnification (D_f/D_s) cannot be more than 20 in this condition. Because the average λ is larger in a helium gas atmosphere than in the air, D_s can be set smaller while

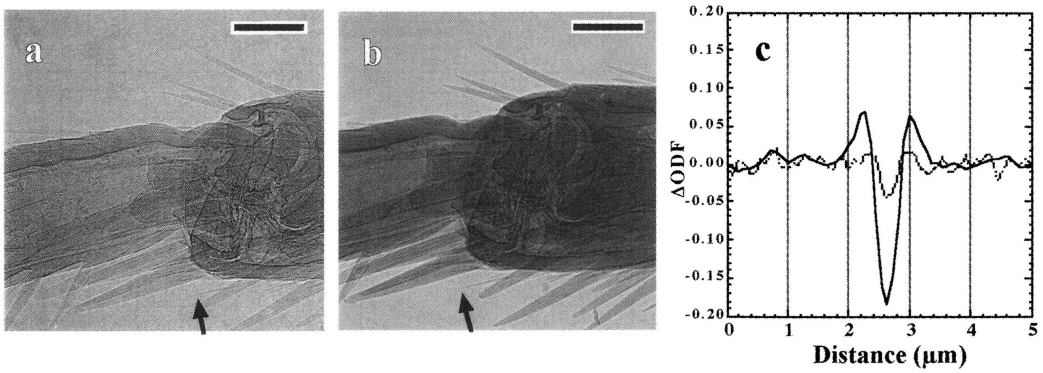

Fig. 4 X-ray micrographs of the thin hairs of an ant leg. The sample chamber was filled with air (a) or helium gas (b). The profiles of the hair shown by the arrows are plotted in c, where the solid line represents helium gas and the dotted line represents air. The vertical axis of c is the relative absorbance (optical density) of the negative film (ODF). Acceleration voltage was 20 keV using a 0.3 μm thick gold target, $D_s=1$ mm and $D_f=120$ mm. Scales = 50 μm.

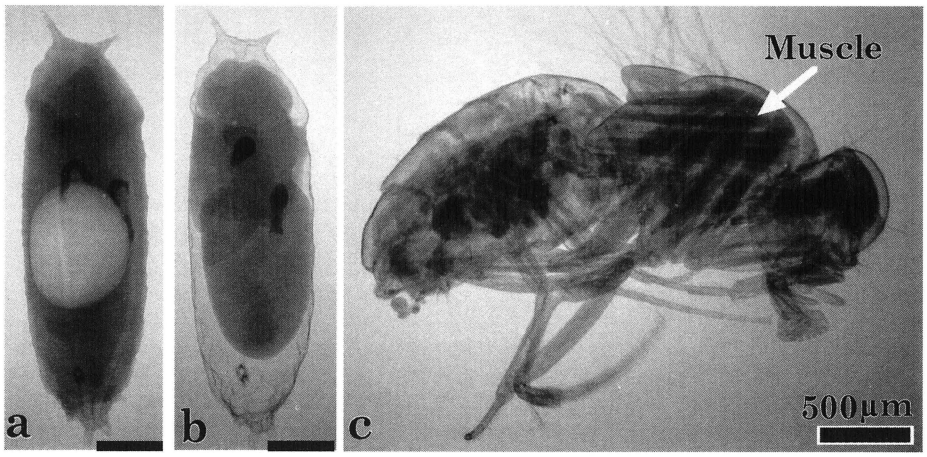

Fig. 5 X-ray micrographs of a single living pupa of *Drosophila melanogaster* during metamorphosis (a, b) and a critical-point dried imago fly (c). a. An oval object in the central part of the pupa indicates a fused portion, 2 h after the pupa formation. b. The oval object disappears and the metamorphosis is almost completed, 39 h after the pupa formation. c. An imago fly treated by critical-point drying. Well-developed flight muscles (arrow) to power the alae can be seen. Acceleration voltage was 20 keV using a 1 μm thick gold target in an air atmosphere, $D_s = 2.5$ mm and $D_f = 30$ mm (cf. Yoshimura *et al.*, 2000). Scales = 500 μm

keeping $D_s\lambda$ at the same value. A stereo-pair micrograph of a Golgi-stained section of rat cerebral cortex recorded at $D_s = 0.4$ mm in helium gas is shown in Figure 7. A 0.2 μm thick gold target with 10 keV acceleration voltage was used, therefore the M_α line ($\lambda = 0.58$ nm) of gold was dominant.

By using longer wave-length X-ray components, the absorption coefficient also increases, if the absorption edge is not in this wave-length range. According to the contrast enhancement produced by the interference and absorption effects, even small biological specimens can be visualized without staining using longer wave-length components. In Figure 8, a stereoscopic view of a water flea, *Moina macrocopa*, is shown. Fine internal structures were clearly

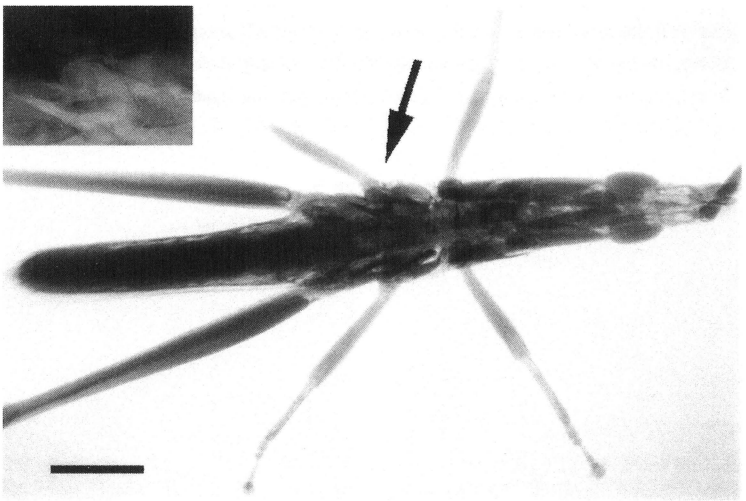

Fig. 6 X-ray micrograph of a grasshopper, *Atractomorpha lata*. Image was recorded in a carbon dioxide gas atmosphere for 10 min exposure time. The inset is the magnified image (negative contrast) around the arrowed area. Acceleration voltage was 20 keV using a 1 μm thick platinum target, $D_s = 5$ mm and $D_f = 50$ mm. Scale = 500 μm.

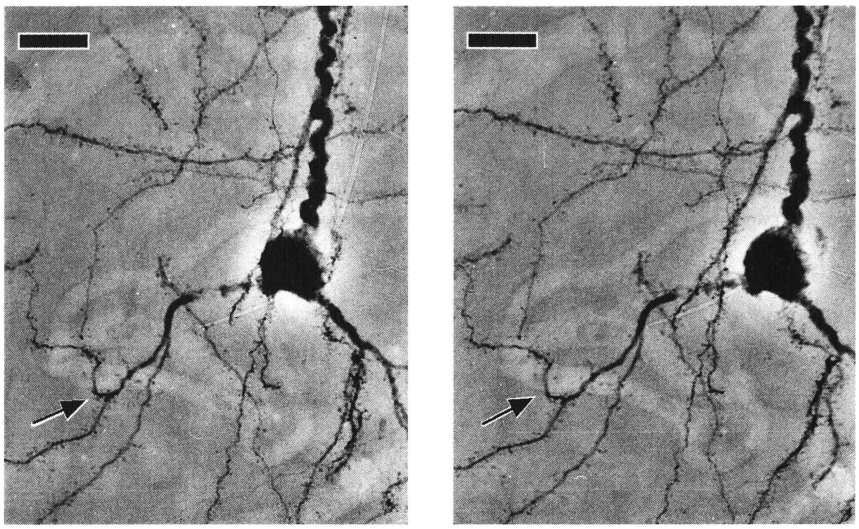

Fig. 7 Stereo X-ray micrograph of rat cerebral cortex. A fixed and stained rat cerebral cortex was cut into 80 μm sections (Hama *et al.*, 1989). A stereo pair was taken by altering the position of the focused electron beam in order to change the viewing angle. The less-stained tube-like structures may be capillary vessels, and a dendrite can be seen to kink around a vessel at the position indicated by the arrow. Acceleration voltage was 10 keV using a 0.2 μm thick gold target, $D_s = 0.4$ mm and $D_f = 30$ mm in helium gas. Scales = 10 μm.

observed. The target metal was 3 μm thick aluminum excited by a 12 keV electron beam. The major X-ray component was aluminum K_α of 8.3 nm. Stereo-pair micrographs were obtained by changing the focus position of the SEM electron beam and hence changing the position of the X-ray light source.

Computed tomography (CT)

Three-dimensional structures can be reconstructed from a set of projection images by means of computed tomography (CT). A convolution backprojection formula for corn-beam CT weighted with a Shepp-Logan filter was used for reconstruction (Feldkamp *et al.*, 1984). Projection images of an isopod, *Porcellio scaber*, of dimension 256×512 pixels, in all directions (360 degrees) were recorded every 1 degree (360 images) with a CCD camera and were used for reconstruction. Some of the sections in the reconstructed three-dimensional image (256×256×512 boxels) are shown in Figure 9. Internal structures such as the digestive tract and muscle-like fiber structures are resolved.

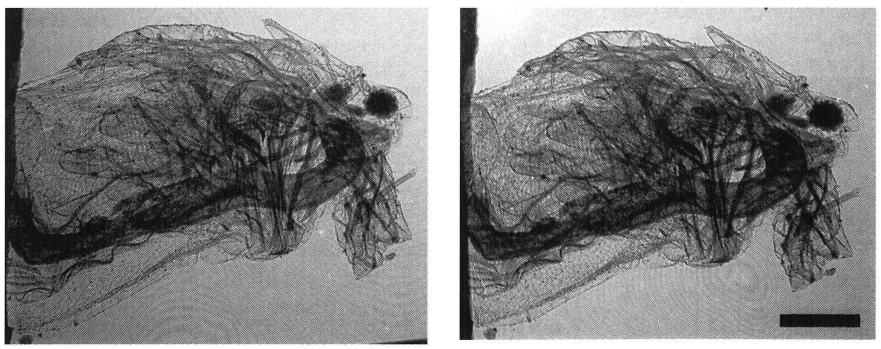

Fig. 8 Stereo X-ray micrograph of a water flea, *Moina macrocopa*. The sample was treated with critical point drying and set on a silicon nitrite support membrane (100 nm thick). Acceleration voltage was 12 keV using a 3 μm thick aluminum target, $D_s = 1.4$ mm and $D_f = 50$ mm. Scale = 100 μm.

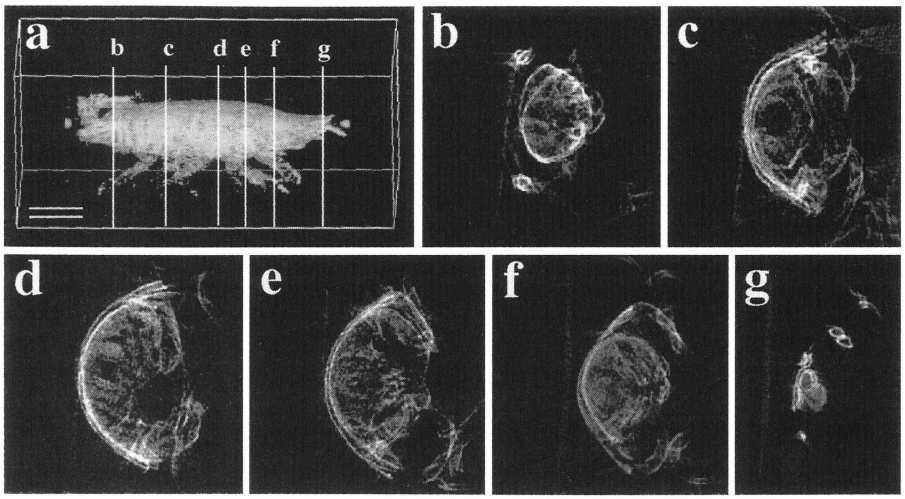

Fig. 9 Sections of the cone beam CT reconstructed image of an isopod, *Porcellio scaber*. The images b to g correspond to the cross section of the 3D image at the position of the surface rendered image shown in a. Dorsal side is positioned in the left (b–g). Scale = 1 mm.

Conclusion

The projection X-ray microscope has the following advantages: (1) easy operation; (2) long focal depth; (3) the internal structure of an optically opaque object can be nondestructively inspected; (4) the resolution is better than that of optical microscopes; (5) wet and living samples can be observed; (6) the X-ray wave length can be changed by changing the target material and the acceleration voltage of electrons, so as to enhance contrast.

By use of the projection X-ray microscope, three-dimensional internal structures of thick and opaque specimens can be visualized in fine resolution without relying on huge facilities.

Acknowledgments: This work is a result of collaboration with Dr. Toshio Mitsui (former Prof. at Meiji University), Mr. Toshihiko Horikoshi, Mr. Hisahiro Chiba, Mr. Shinya Kumagai, Mr. Daisuke Shoutsu, Mr. Ryuji Sano, Ms. Chiaki Kuzuryu, Mr. Chikara Miyata, Mr. Hiroshi Maeda, Ms. Ayumi Hori, Mr. Hidekazu Takada, Mr. Keisuke Igarashi, and Mr. Tsutomu Miyazaki (Graduate and undergraduate students, Meiji University). The author is much indebted to Dr. Keiji Yada for his helpful suggestions during the construction of the microscope. The author is also grateful to Dr. Takashi Obi and Dr. Nagaaki Ohyama (Tokyo Institute of Technology, Yokohama) for discussion concerning the CT technique.

References

Anderson, T.F. (1951) Techniques for the preservation of three-dimensional structure in preparing specimens for the electron microscope. *Trans. N. Y. Acad. Sci.*, **13**, 130–134.

Cosslett, V.E. and W.C. Nixon (1951) X-ray shadow microscope. *Nature*, **168**, 24–25.

Feldkamp, L.A., L.C. Davis and J.W. Kress (1984) Practical cone-beam algorithm. *J. Opt. Soc. Am., A*, **1**, 612–619.

Hama, K., T. Arii and T. Kosaka (1989) Three-dimensional morphometrical study of dendritic spines of the granule cell in the rat dentate gyrus with HVEM stereo images. *J. Electron Microsc. Tech.*, **12**, 80–87.

Lonsdale, K. (1968) *International Tables for X-ray Crystallography, Vol. III*. The Kynoch Press, Birmingham.

Newberry, S.P. (1988) Image capture in the projection shadow X-ray microscope. *In* D. Sayre, M. Howells, J. Kirz and H. Rarback (eds.), *X-ray Microscopy II, Optical Sciences, Vol. 56*, pp. 306–309. Springer-Verlag, Berlin.

Newberry, S.P. and S.E. Summers (1956) The General Electric shadow X-ray microscope. *Proc. Int. Conf. Electron Microsc. (1954)*, 305–307.

Nixon, W.C. (1955) High-resolution X-ray projection microscopy. *Proc. R. Soc. Lond., Ser. A*, **232**, 475–485.

Wilkins, S.W., T.E. Gureyev, D. Gao, A. Pogany and A.W. Stevenson (1996) Phase-contrast imaging using polychromatic hard X-rays. *Nature*, **384**, 335–338.

Yada, K. and S. Takahashi (1988) A projection X-ray microscope converted from a scanning electron microscope, and its applications. *In* D. Sayre, M. Howells, J. Kirz and H. Rarback (eds.), *X-ray Microscopy II, Optical Sciences, Vol. 56*, pp. 323–326. Springer-Verlag, Berlin.

Yoshimura, H., S. Kumagai, D. Shoutsu, Y. Sekiya and T. Mitsui (1997) Phase contrast in a projection X-ray microscopy and time resolved imaging. *Cell Vision*, **4**, 210–211.

Yoshimura, H., D. Shoutsu, T. Horikoshi, H. Chiba, S. Kumagai, K. Takahashi and T. Mitsui (2000) Application of SEM-modified X-ray microscope to entomology and histology, and effects of X-ray coherence in imaging. *J. Electron Microsc.*, **49**, 621–628.